Supporting information

Active nanorheology with plasmonics

Hyeon-Ho Jeong^{1,2,‡}, Andrew G. Mark^{1,‡}, Tung-Chun Lee^{1,3}, Mariana Alarcón-Correa^{1,4}, Sahand Eslami^{1,4}, Tian Qiu^{1,5}, John G. Gibbs^{1,6}, and Peer Fischer^{1,4,*}

 ¹Max Planck Institute for Intelligent Systems, Heisenbergstrasse 3, 70569 Stuttgart, Germany
 ²Institute of Materials, École Polytechnique Fédérale de Lausanne (EPFL), CH-1015 Lausanne, Switzerland
 ³ UCL Institute for Materials Discovery and Department of Chemistry, University College London,

Christopher Ingold Building, 20 Gordon Street, London WC1H 0AJ, United Kingdom

⁴Institute for Physical Chemistry, University of Stuttgart, Pfaffenwaldring 55, 70569 Stuttgart,

Germany

⁵Institute of Bioengineering, École Polytechnique Fédérale de Lausanne (EPFL), CH-1015 Lausanne, Switzerland

⁶ Department of Physics and Astronomy, Northern Arizona University, S. San Francisco Street,

Flagstaff, Arizona 86011, USA

[‡]These authors contributed equally

*Corresponding author (fischer@is.mpg.de)

Keywords: magneto-plasmonics, chiral plasmonics, chiroptical switch, nanorheology

Supplementary Videos:

Supplementary Video 1: Observation of the Brownian motion of the colloidal Au-Fe nanohelices in water (upper panel) and 50% glycerol-water mixture (lower panel) in a dark-field optical microscope.

Supplementary Video 2: Observation of the aligned Au-Fe nanohelices along the directions of the external magnetic fields at $\mathbf{B} = 5$ mT parallel to the x-axis ($\theta_{\mathbf{B}} = 0^{\circ}$, upper panel) and parallel to the y-axis ($\theta_{\mathbf{B}} = 90^{\circ}$, lower panel) in 50% glycerol-water mixture in a dark-field optical microscope.

Supplementary Video 3: Observation of the rotation of the Au-Fe nanohelices in the presence of a continuously modulated magnetic field at different frequencies: Brownian motion (top left), $f_{\rm B} = 0.1$ Hz (top right), 0.5 Hz (bottom left), and 1 Hz (bottom right).

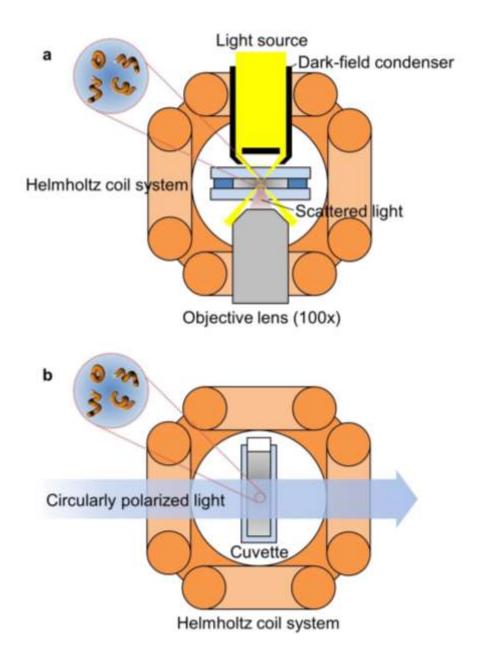


Figure S1: Schematic views of the experimental setups. (a) An inverted dark-field optical microscope with a 3D Helmholtz coil system. (b) A commercial CD spectrometer (not shown) combined with a 3D Helmholtz coil system.

Supplementary Note S1: Characterization of the chiral magneto-plasmonic nanohelix

Au-Fe nanohelices were grown on an array of the Au nanoparticles, patterned by BCML, in our nanoGLAD system¹, Figures S2a-c. Its compositional analysis was performed using scanning TEM (STEM) imaging with energy-dispersive X-ray spectroscopy (EDX) measurements. Figure 2c shows the STEM image of a single two-turn left-handed Au-Fe nanohelix and corresponding images of EDX false-color elemental maps of Au, Fe, and O, respectively, which reveal nanoscale mixing between Au and Fe. The atomic ratio of Au to Fe was approximately 46.7:53.3 (\pm 1.8%) based on integrated EDX intensity. This is consistent with measurements from inductively coupled plasma atomic emission spectroscopy (ICP-OES) which indicates a ratio of 40.8:59.2 (\pm 6.1%). Figure S3 shows the Auger depth profile of the Au-Fe nanohelices on Si wafer (similar to what is shown in Figure S2b) as a function of the etching time (i.e. depth) by Ar plasma. The low oxygen signal during the b phase relative to the a phase suggests that the oxygen is confined to the nanoparticles' surface. The structural dimensions of (left-handed) Au-Fe nanohelices are deduced from transmission electron microscopy (TEM) images of 100 individual nanohelices. (See Figure S4 and Supplementary Table 1).

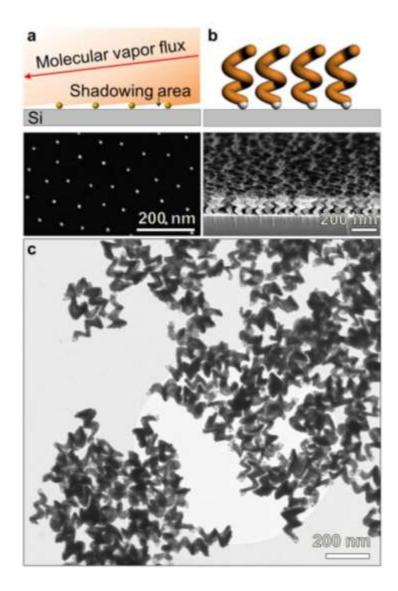


Figure S2: (a) nanoGLAD onto a surface seeded with Au nanodots (BCML). Lower panel shows a top view SEM image of an array of Au nanoparticles 12 nm in diameter and with 100 nm gaps between nanoparticles. (b) Growth of 2-turn Au-Fe nanohelices on a Au/SiO₂ array using nanoGLAD. Lower panel shows the corresponding SEM image (tilted view) of the 2-turn Au-Fe nanohelices ~170 nm in height. (c) Large-area TEM image of Au-Fe 2-trun left-handed nanohelices.

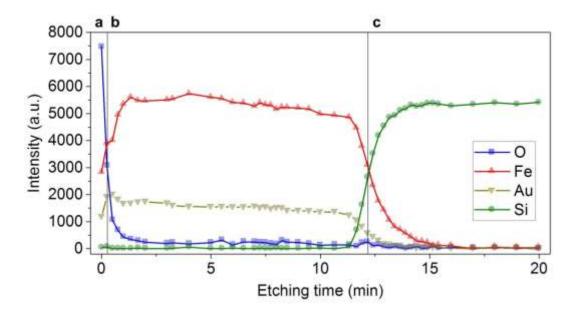


Figure S3: Auger depth profiling of the Au-Fe nanohelix as a function of the etching time by Ar plasma. Auger electron scattering intensities of O (blue square), Fe (red top triangle), Au (yellow bottom triangle), and Si (green circle) according to the regions of (a) a native oxide layer on top of the helix, (b) a body of the Au-Fe helix, and (c) a Si substrate.

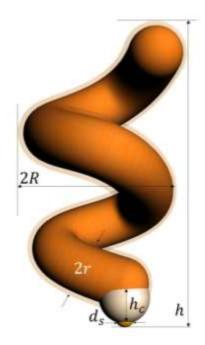


Figure S4: Schematic view of 2-turn left-handed nanohelix showing dimensions of the seed particle and the nanostructure that grows upon it.

2 turn left hand helices	d _s	h _c	h	2 <i>r</i>	2 <i>R</i>
Mean [nm]	12.1	9.2	168.8	28.3	82.9
Standard deviation [nm]	1.8	2.9	8.4	4.1	9.3
Percentage Standard deviation [%]	14.9	31.5	5.0	14.5	11.2

Supplementary Table 1: Statistical analysis of 100 individual Au-Fe 2-turn left-handed nanohelices.

Supplementary Note S2: Magnetic alignment of nanohelix

To completely align a nanohelix with the external magnetic field **B**, the magnitude of the magnetic field strength can be estimated by considering $m_r \mathbf{B} > k_B T$, where m_r is the remanence of a single Au-Fe nanohelix in Figure 2d (1.174×10⁻¹⁴ emu), **B** is the magnetic field strength, k_B is the Boltzmann constant (1.38×10⁻²³ J·K⁻¹), and *T* is the temperature (here 300K). Therefore, the minimum external magnetic field \mathbf{B}_m strength is given by

$$\mathbf{B}_{\mathbf{m}} = \frac{k_B T}{m_r} = \sim 0.4 \text{ mT} \tag{1}$$

This suggests that the Au-Fe nanohelices can be aligned to the external magnetic field of $\mathbf{B} > 0.4 \text{ mT}$ (40 G). To test that the helix is properly aligned by the field $\mathbf{B}_{\mathbf{m}}$, we have observed individual nanohelices in solution by using (1) SEM, (2) DF, and (3) CD. (1) For the SEM analysis, a colloidal solution of Au-Fe nanohelices was drop-cast on a clean Si support and exposed to an external magnetic field with a permanent magnet for ~ 5 min. Then, the solution was rapidly dried with N₂ gas and the solution vacuum dried. Figure S5 shows the SEM images, which clearly show that the (long axes of the) nanohelices are aligned along the magnetic field. (2) Using the dark-field optical microscope, we can observe the alignment of the helix in real-time. The Au-Fe nanohelices were suspended in 50% glycerol in water (to suppress the Brownian motion) and exposed to the static (Supplementary Video 2) or rotating (Supplementary Video 3) magnetic field at $\mathbf{B} = 5$ mT and, again, the long axis of the nanohelices was well aligned parallel to the direction of the magnetic field. (3) Finally, we have measured the chiroptical responses of the colloidal Au-Fe nanohelices under the static magnetic field (red: $\mathbf{B} \parallel \mathbf{k}$, violet: $\mathbf{B} \perp \mathbf{k}$) with different intensities ranging from 0.5 to 7 mT. Figure S6 shows the chiroptical responses at $\lambda = 880$ nm of the colloidal Au-Fe nanohelices as a function of the magnetic field strength. Again, most of the nanohelices can be aligned with a magnetic field of at least $\mathbf{B} \sim 1 \text{ mT}$.

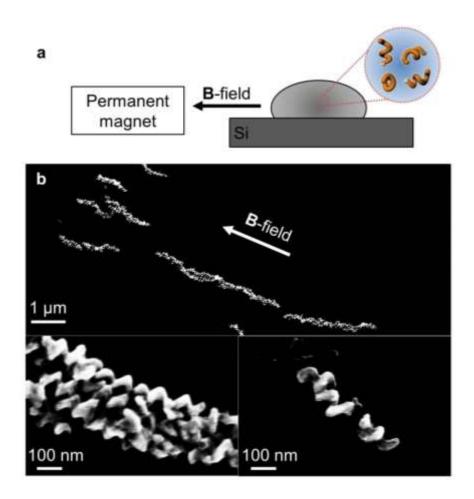


Figure S5: Visualization of the magnetic anisotropy of the Au-Fe nanohelices. (a) An experimental scheme and (b) its resultant SEM image.

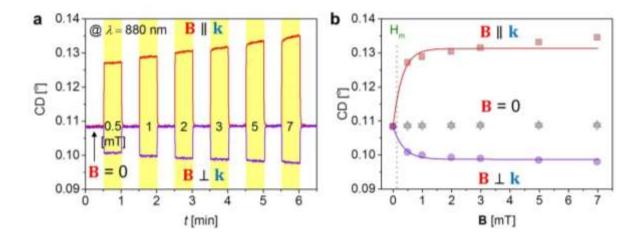


Figure S6: (a) Chiroptical responses of the colloidal Au-Fe nanohelices at $\lambda = 880$ nm in the presence of a static magnetic fields along $\theta_{\mathbf{B}} = 0^{\circ}$ (red line) and $\theta_{\mathbf{B}} = 90^{\circ}$ (violet line). The strength of the magnetic field ranges from 0.5 to 7 mT. (b) The corresponding chiroptical responses re-plotted as a function of the magnetic field intensity.

Supplementary Note S3: Translational Brownian diffusion coefficient of nanohelix

By comparing the theoretical and experimental translational diffusion coefficients D_t of the nanohelix, we can evaluate whether a single nanohelix is observed through the dark-field optical microscope. We tracked the centroid positions of 10 nanohelices in fluids with two different viscosities for 10 sec at 20 frames sec⁻¹ and calculated the translational Brownian diffusion coefficient D_t (= MSD/4t), where MSD is the mean squared displacement of the nanoparticles, Figures S7a-e^{2,3}. This gave $D_t = 2.38 \pm 0.05 \ \mu\text{m}^2 \cdot \text{sec}^{-1}$ in pure water and $D_t = 0.37 \pm 0.01 \ \mu\text{m}^2 \cdot \text{sec}^{-1}$ in a 50% glycerol-water mixture, which were analytically calculated using a MATALB code developed by our group², Figure S7e (See also Supplementary Video 1). By considering the geometry of the nanohelix as an ellipsoid with an aspect ratio (AR) of 2 (h/2R), we can estimate the theoretical D_t of the nanohelix from the Einstein-Smoluchowski relation as⁴

$$D_t = \frac{(D_a + D_b)}{2} \tag{2}$$

where D_a is the diffusional coefficient at the long axis of the ellipsoid *a* and D_b is the diffusional coefficient at the short axis of the ellipsoid *b*. When $AR(a/b) \gg 1$, where D_a and D_b are given as⁵

$$D_a = \frac{k_B T \ln AR}{2\pi\eta a} \tag{3}$$

$$D_b = \frac{k_B T \ln AR}{4\pi\eta a} \tag{4}$$

where the viscosity of the solution, η is 1.0049 cP for water and 8.3968 cP for the 50% glycerol-water mixture⁶. Thereby, D_t is 3.5 μ m²/sec in water and 0.38 μ m²/sec for 50% glycerol in water, in good agreement with the measured values. This indicates that the tracked nanohelices act as discrete particles undergoing Brownian motion.

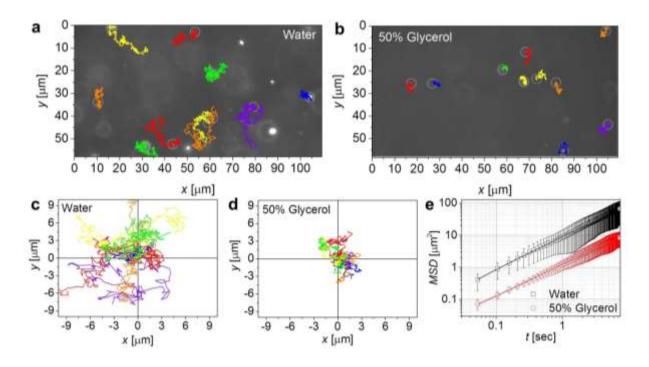


Figure S7: Brownian motion of the Au-Fe left-handed nanohelices in (a) water and (b) 50% glycerol in water as observed by single particle tracking using dark-field optical microscopy. Each image shows 10 nanoparticle trajectories, where each trajectory's start position is set to (x = 0, y = 0) in (c) water and (d) 50% glycerol in water. (e) Corresponding MSDs of Au-Fe nanohelices plotted as a function of time (black square: water, red circle: 50% glycerol).

Supplementary Note S4: Molar CD

For the evaluation of the molar CD of the Au-Fe nanocolloids, we calculated the molar concentration of colloidal nanohelices in 1 mL solution as 20.3 pM. The molar CD of the colloidal nanohelices is given as⁷,

$$Molar CD = CD/c \cdot l \left[{}^{\circ} \cdot M^{-1} \cdot cm^{-1} \right]$$
(5)

where *c* is the molar concentration of the colloidal nanohelices, *l* is the optical path length of the cuvette (l = 0.5 cm). Figure S8 shows the molar CDs of the colloidal Au-Fe nanohelices for the different $\theta_{\rm B}$ plotted as a function of λ .

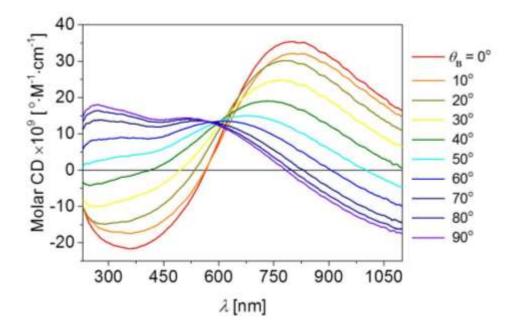


Figure S8: Chiroptical responses of the colloidal Au-Fe left-handed nanohelices in Figure S9a replotted with the y-axis of the molar CD.

Supplementary Note S5: DDSCAT

For the numerical calculation of the Au-Fe nanohelices CD spectrum, we first calculated the dielectric function of Au-Fe as a function of wavelength based on the optical constants provided by Palik⁸. An atomic ratio of 1:1.5 of Au:Fe was assumed which is based on the ICP-OES results. The chiroptical response of the Au-Fe nanohelix alloy was computed using the DDASCAT 7.2⁹. The scattering and absorption of 2-turn left-handed helices were calculated for a geometry that is based on the statistical analysis of the TEM images of the 100 individual nanohelices. The helix is modelled as an array of polarizable point dipoles spaced 2.161 nm apart, and we calculated their interactions using the code developed by our group, Figure S9^{1, 10}.

The optical response was computed by DDSCAT by averaging 342 orientations $(18\theta \times 19\beta)$ of the Au-Fe nanohelix across the wavelength range from 200 nm to 1,100 nm. θ and β are the rotational angles of the long-axis and short-axis of the helix respectively.

The application of the external magnetic field in the experiment constrains the helix's θ rotation, but not its rotation about β . Thereby, for the comparison between the calculation and experiment, the theoretical CD spectra have been recalculated as

$$CD_{exp}(\theta_{\mathbf{B}}) = \langle CD_{cal}(\theta) \rangle_{\beta}$$
(6)

and both are plotted in Figure S10.

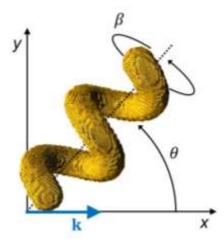


Figure S9: Arrangements of dipoles with 2.161 nm spacing according to the statistical analysis of the Au-Fe nanohelix geometry.

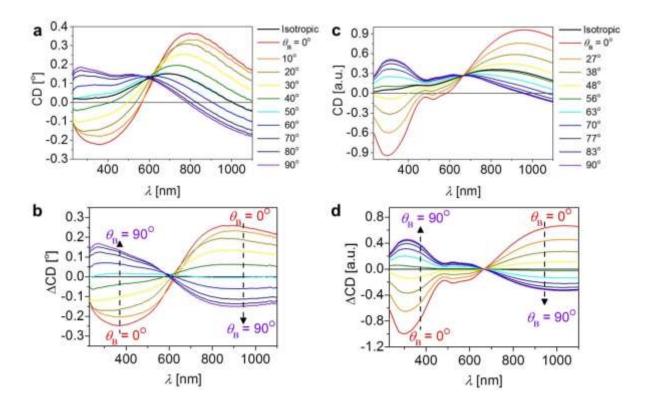


Figure S10: Experimental and theoretical chiroptical responses of the Au-Fe left-handed nanohelices as functions of λ and $\theta_{\mathbf{B}}$. (a) The measured CDs of colloidal Au-Fe left-handed nanohelices at $\mathbf{B} = 1$ mT with $\theta_{\mathbf{B}}$ ranging from 0° to 90° in 10° intervals. (b) Their corresponding Δ CDs plotted as a function of λ . (c) The numerically calculated CDs of Au-Fe left-handed nanohelices plotted as a function of λ by varying the $\theta_{\mathbf{B}}$ ranging from 0° to 90°. (d) Their corresponding Δ CDs plotted as a function of λ .

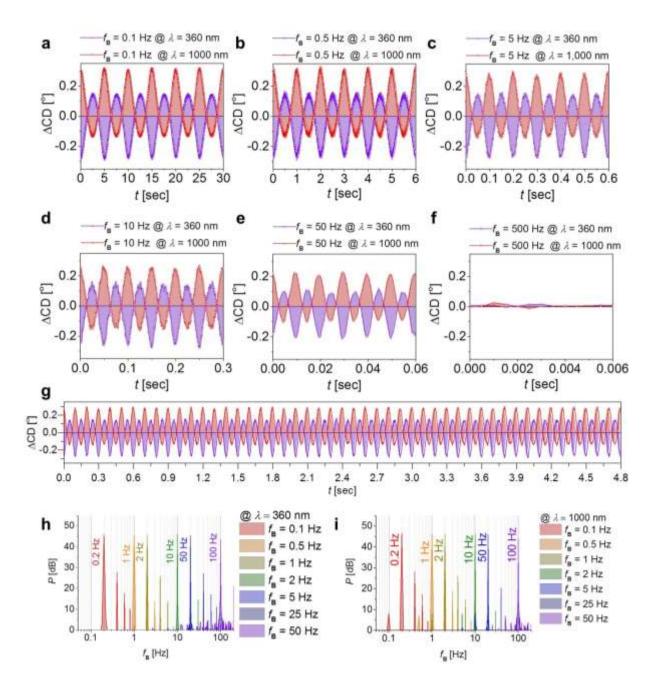
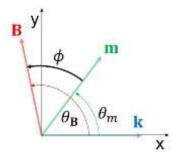


Figure S11: Δ CDs of the colloidal Au-Fe left-handed nanohelices at $\lambda = 360$ nm (violet line) and 1,000 nm (red line) for **B** = 1 mT at $f_{\mathbf{B}} =$ (a) 0.1 Hz, (b) 0.5 Hz, (c) 5 Hz, (d) 10 Hz, (e) 50 Hz, and (f) 500 Hz. (g) A continuous modulation of the Δ CDs at $f_{\mathbf{B}} = 0.5$ Hz. The FFT analysis on the corresponding chiroptical response at (h) $\lambda = 360$ nm and (i) 1,000 nm. Each label indicates the frequency f_{CD} that is coincident with $2f_{\mathbf{B}}$.

Supplementary Note S6: Viscosity sensing

In order to derive an equation that describes the nanorheology of our particle system, we have applied and adapted the theory for the hydrodynamic response of magnetic nanorods¹¹.



At steady state, the torque due to hydrodynamic drag will be balanced by the applied magnetic torque:

$$\boldsymbol{\tau}_{\boldsymbol{D}} = \boldsymbol{\tau}_{\mathbf{B}}$$
$$\boldsymbol{\chi}\boldsymbol{\eta}\boldsymbol{\omega} = \mathbf{m} \times \mathbf{B} \tag{7}$$

where χ is the hydrodynamic shape constant (for a sphere $\chi = 8 \pi R^3)^{12}$, η is the dynamic viscosity of the medium, **B** is the vector of the applied magnetic field, and **m** is the vector of the magnetic moment along the long axis of the nanohelix. ω is the angular velocity of the nanohelix which is given as

$$\omega = \frac{d\theta_m}{dt} \tag{8}$$

where θ_m is the angle between **m** and the wave vector **k** of the incident light. By considering the angular function $\theta_{\mathbf{B}} = 2\pi f_{\mathbf{B}}t$ and $\phi = \theta_{\mathbf{B}} - \theta_m$ where θ_B is the angle between **B** and **k**, $f_{\mathbf{B}}$ is the frequency of the applied rotating magnetic field, Eq.(8) can be written as

$$\frac{d\theta_m}{dt} = 2\pi f_{\mathbf{B}} - \frac{d\phi}{dt} \tag{9}$$

For a steady rotational of the nanohelix (i.e., below the step-out frequency) $d\phi/dt$ is zero and Eq. (7) can be rewritten as

$$\sin\phi = \frac{2\pi\chi\eta}{m_r \mathbf{B}} f_{\mathbf{B}} \tag{10}$$

For a given magnetic field strength and a frequency below the step-out, the 1st derivative $dsin \phi / df_B$ is a function of the viscosity,

$$\frac{d\sin\phi}{df_{\rm B}} = \frac{2\pi\chi}{m_r {\rm B}}\eta\tag{11}$$

Figure S12 shows the schematic view of the designed phase sensitive detection system with the integrations of two lock-in amplifiers. The first lock-in-amplifier (LIA 1) reduces the noise level of the chiroptical response containing f_{CD} component by referencing the signal from the photomultiplier (PMT) to the photoelastic modulator (PEM) which modulates the light from left- to right-circularly polarized. The second lock-in LIA2 references this signal to the f_B from the coil system. LIA2 thus provides the phase difference between the optical response and the applied magnetic field. Since the measured phase angle ϕ' also contains a phase lag due to the inductance phase lag of the coil system ϕ_L , and the initial chiroptical phase lag ϕ'_0 , one obtains the resultant geometrical phase lag ϕ :

$$\phi = \frac{1}{2}\phi' - \phi'_0 - \phi_L \tag{12}$$

The calibrated phase lag ϕ , which is small and expressed in radians, can be fitted by a 2nd order polynomial function. For example, in the case of water ($\eta = 1.0049$ at T = 20°C), the phase is approximately given as

$$\sin\phi \sim \phi \sim 0.0085 + 0.0304 f_{\rm B} \tag{13}$$

Based on Eq. (13), we can obtain the 1st derivative $(dsin \phi/df_B)$,

$$\frac{d\sin\phi}{df_{\rm B}} = 0.0304\tag{14}$$

Calibration measurements for glycerol-water mixtures of differing viscosities (see Figure S13) are used to obtain a reference curve for the absolute dynamic viscosity,

$$\frac{d\sin\phi}{df_{\rm B}} = 0.00241\eta + 0.02787\tag{15}$$

Figure 4b shows the experimental values of $d\sin\phi \cdot df_{\rm B}^{-1}$ as a function of the theoretical viscosity, η of the glycerol-water mixture. With its 2nd derivative $d^2\sin\phi \cdot df_{\rm B}^{-1} d\eta^{-1}$ we can calculate the shape constant, χ

$$\chi = 0.00241 \frac{m_r \mathbf{B}}{2\pi} = 1.35 \times 10^7 \text{ nm}^3 \tag{16}$$

An order of magnitude estimate of this quantity can be calculated by modelling our helix as a cylinder. In this case the shape constant is given by ¹³,

$$\chi = \frac{\pi l^3}{3 \operatorname{g}\left(\frac{l}{d}\right)} \tag{17}$$

where $g\left(\frac{l}{d}\right) = \ln\left(\frac{l}{d}\right) - 0.662 + 0.917\frac{l}{d} - 0.050\left(\frac{l}{d}\right)^2$.¹⁴ With a length l = 168.8 nm and diameter d = 82.9 nm this predicts a shape constant of $\chi = 2.95 \times 10^6$ nm³.

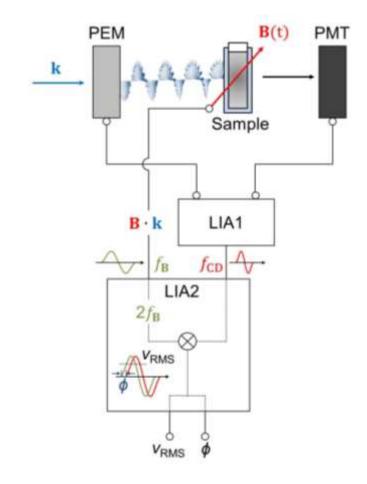


Figure S12: Schematic diagram of the phase sensitive chiroptical measurement system.

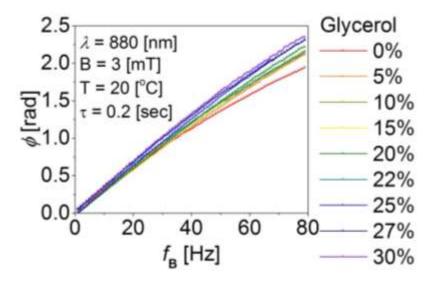


Figure S13: Phase angle, ϕ of the colloidal Au-Fe nanohelices for glycerol-water mixtures of differing concentrations and hence viscosities, as a function of $f_{\mathbf{B}}$ at $\mathbf{B} = 3 \text{ mT}$, $\lambda = 880 \text{ nm}$ and $T = 20^{\circ}\text{C}$.

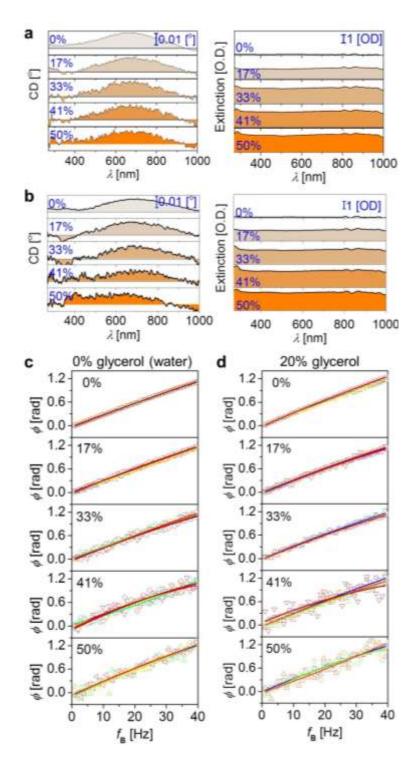


Figure S14: In situ nanorheology measurements with colloidal Au-Fe nanohelices in glycerol-water mixtures in the presence of different concentrations of polystyrene microspheres. CD (left panel) and extinction (right panel) spectra of the colloidal Au-Fe nanohelices in (a) water and (b) 20% glycerol-water mixture surrounded by the polystyrene microspheres. The ϕ measurements as a function of $f_{\rm B}$ at $\lambda = 880$ nm, ${\rm B} = 3$ mT and T = 20°C in the presences of (c) water and (d) 20% glycerol-water mixture.

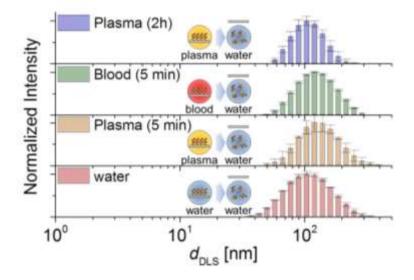


Figure S15: DLS measurements of the colloidal Au-Fe nanohelices in the presence of water after different pre-treatments in water (red), blood plasma (orange, for 5 min and blue, for 2h), and whole blood (green).

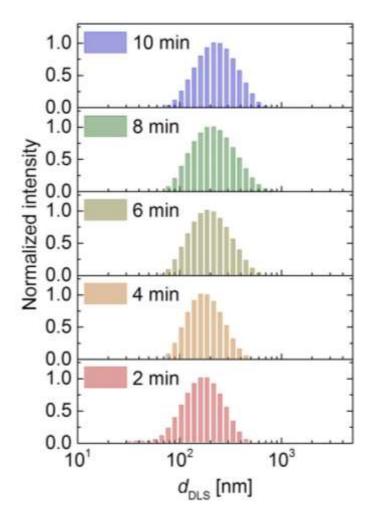


Figure S16: DLS measurements of the colloidal Au-Fe nanohelices in $1 \times$ phosphate buffer saline (PBS) solution at the specified times (red: 2 min, orange: 4 min, yellow: 6 min, green: 8 min, and blue: 10 min) after sonication.

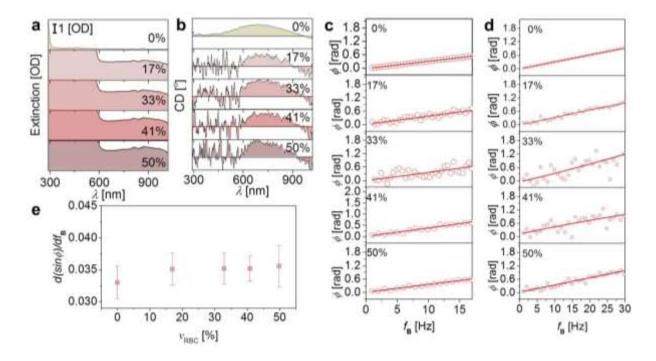


Figure S17: (a) Extinction and (b) CD spectra of the colloidal Au-Fe nanohelices in the presence of different hematocrit levels. *In situ* nanorheology of bovine blood plasma in the presence of different concentrations of the erythrocytes. Measurements using colloidal Au-Fe nanohelices ((c) cattle A and (d) cattle B). (e) Their corresponding averaged $d\sin\phi/df_B$ as a function of the haematocrit volume fraction.

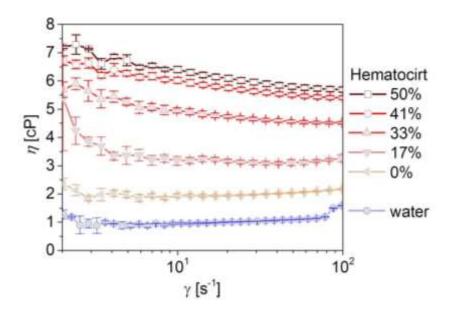


Figure S18: Macro rheology of bovine whole blood with different concentrations of erythrocytes using a commercial viscometer at shear rates ranging from 2 to 100 s^{-1} at 20° C.

References

- 1. Mark, A. G.; Gibbs, J. G.; Lee, T.-C.; Fischer, P. Nat Mater 2013, 12, (9), 802-807.
- 2. Lee, T.-C.; Alarcón-Correa, M.; Miksch, C.; Hahn, K.; Gibbs, J. G.; Fischer, P. Nano Letters 2014, 14, (5), 2407-2412.
- 3. Schamel, D.; Mark, A. G.; Gibbs, J. G.; Miksch, C.; Morozov, K. I.; Leshansky, A. M.; Fischer, P. ACS Nano 2014.
- 4. Han, Y.; Alsayed, A.; Nobili, M.; Yodh, A. G. *Physical Review E* 2009, 80, (1), 011403.
- 5. Happel, J.; Brenner, H., Low Reynolds number hydrodynamics: with special applications to particulate media. Springer Netherlands: 1983.
- 6. Cheng, N.-S. Industrial & Engineering Chemistry Research 2008, 47, (9), 3285-3288.
- McPeak, K. M.; van Engers, C. D.; Blome, M.; Park, J. H.; Burger, S.; Gosálvez, M. A.; Faridi, A.; Ries, Y. R.; Sahu, A.; Norris, D. J. *Nano Letters* 2014, 14, (5), 2934-2940.
- 8. Palik, E. D., Handbook of Optical Constants of Solids. Elsevier Science: 1985.
- 9. Draine, B. T.; Flatau, P. J. J. Opt. Soc. Am. A 1994, 11, (4), 1491-1499.
- 10. Gibbs, J. G.; Mark, A. G.; Eslami, S.; Fischer, P. Applied Physics Letters 2013, 103, (21), -.
- 11. Tokarev, A.; Aprelev, A.; Zakharov, M. N.; Korneva, G.; Gogotsi, Y.; Kornev, K. G. *Review of Scientific Instruments* **2012**, 83, (6), 065110.
- 12. Eric, L.; Thomas, R. P. Reports on Progress in Physics 2009, 72, (9), 096601.
- 13. Colin, R.; Yan, M.; Chevry, L.; Berret, J. F.; Abou, B. *EPL (Europhysics Letters)* **2012**, 97, (3), 30008.
- 14. Berret, J. F. Nat Commun 2016, 7.